REPORT DOCUMENTATION PAGE

Form Approved
OMB No. 0704-0188

1. AGENCY USE ONLY (Leave blank)	2. REPORT DATE	3. REPORT TYPE AND DATES COVERED
	March 20, 1997	Final Technical Report

4. TITLE AND SUBTITLE
Characterization of high-speed impinging jets in a high pressure and temperature environment

5. FUNDING NUMBERS
PE-61102F
PR-2308
SA-AS
G-F49620-94-1-0347

6. AUTHOR(S)
PI: Dimos Poulikakos

7. PERFORMING ORGANIZATION NAME(S) AND ADDRESS(ES)
Mechanical Engineering Dept.
University of Illinois at Chicago
842 W.Taylor Str.
Chicago, IL 60607

AFOSR-TR-97

0158

9. SPONSORING/MONITORING AGENCY NAME(S) AND ADDRESS(ES)
AFOSR?NA
110 Duncan Avenue, Suite B115
Bolling AFB, DC 20332-8080

NA

10. SPONSORING/MONITORING AGENCY REPORT NUMBER
94-1-0347

11. SUPPLEMENTARY NOTES

12a. DISTRIBUTION/AVAILABILITY STATEMENT
Approved for public release; distribution is unlimited

12b. DISTRIBUTION CODE

19970602 127

13. ABSTRACT *(Maximum 200 words)*

The purpose of this work is to study the dense region of two high-speed impinging jets in a temperature and pressure environment that is above atmospheric conditions. The program was terminated one year short due to the departure of the PI from the US. Nevertheless all of the goals that were set for this time period were accomplished. The measurements were performed using a double pulse, two reference beam holographic technique. The working fluids utilized were water, a 59% weight percent aqueous glycerol solution, and ethanol. Velocity measurements and drop-size distributions were obtained for various regions of the spray, and the universal root-normal distribution was used as a representation of the cumulative volume distributions. Generally, the qualitative nature of the spray pattern remained the same as temperature increased, however, the size of the resulting droplets decreased as a result of evaporation and increased instabilities. Furthermore, the wave structure, which is characteristic of a fully developed impinging jet spray, became less distinct as temperature increased. Two mechanisms combined to reduce the drop diameters. First, as temperature increases, the viscosity of the air increases and the viscosity of the spray fluid decreases; thus, the larger spray structures atomize earlier due to the magnification of aerodynamic instabilities. Second, the heat up of the droplets, which is facilitated by the earlier primary atomization, leads to the evaporation of particle mass, and in the case of the smallest droplets, complete vaporization. Furthermore, the interaction of these two factors causes the representative diameters to increase with temperature over a small range of temperatures beyond the boiling point as the smaller droplets decrease and dissappear faster than the larger droplets. At downstream locations, the average droplet velocity decreased to approximately 65% of the mean jet velocity.

14. SUBJECT TERMS	15. NUMBER OF PAGES
-holography -sprays -liquid propulsion engines	32
	16. PRICE CODE

17. SECURITY CLASSIFICATION OF REPORT	18. SECURITY CLASSIFICATION OF THIS PAGE	19. SECURITY CLASSIFICATION OF ABSTRACT	20. LIMITATION OF ABSTRAC
unclassified	unclassified	unclassified	UL

CONTENTS

CHARACTERIZATION OF HIGH-SPEED IMPINGING JETS IN A HIGH PRESSURE AND TEMPERATURE ENVIRONMENT

Grant No. : F49620-94-1-0347

Principal Investigator : Prof. Dimos Poulikakos

Mechanical Engineering Department
University of Illinois at Chicago
842 W. Taylor Street
Chicago IL 60607-7022
Tel: (312) 996-5239 Fax: (312) 413-0447
e-mail: dimos@dimos.me.uic.edu

SUMMARY

The purpose of this work is to study the dense region of two high-speed impinging jets in a temperature and pressure environment that is above atmospheric conditions. In the two years of the research the efforts focused on completing the construction of the experimental setup and thoroughly documenting the effect of increasing the environment temperature on the atomization process. The program was terminated one year short due to the departure of the PI from the US. Nevertheless all of the goals that were set for this time period were accomplished. The impinging jet spray was formed by a pair of 0.8 mm jets impinging at an angle of 90° at ambient temperatures from 25°C to 250°C. The measurements were performed using a double pulse, two reference beam holographic technique. The working fluids utilized were water, a 59% weight percent aqueous glycerol solution, and ethanol. Velocity measurements and drop-size distributions were obtained for various regions of the spray, and the universal root-normal distribution was used as a representation of the cumulative volume distributions. Generally, the qualitative nature of the spray pattern remained the same as temperature increased, however, the size of the resulting droplets decreased as a result of evaporation and increased instabilities. Furthermore, the wave structure, which is characteristic of a fully developed impinging jet spray, became less distinct as temperature increased. Two mechanisms combined to reduce the drop diameters. First, as temperature increases, the viscosity of the air increases and the viscosity of the spray fluid decreases; thus, the larger spray structures atomize earlier due to the magnification of aerodynamic instabilities. Second, the heat up of the droplets, which is facilitated by the earlier primary atomization, leads to the evaporation of particle mass, and in the case of the smallest droplets, complete vaporization. Furthermore, the interaction of these two factors causes the representative diameters to increase with temperature over a small range of temperatures beyond the boiling point as the smaller droplets decrease and disappear faster than the larger droplets. The average velocity of the particles within a 20° envelope of the spray center line in the dense region was approximately equal to the mean jet velocity. At downstream locations, the average droplet velocity decreased to approximately 65% of the mean jet velocity.

Nomenclature

$D_{0.5}$	mass median diameter
D_{32}	Sauter mean diameter
D_j	liquid jet diameter
D_N	normalized droplet diameter
V_j	liquid jet velocity
Q	cumulative liquid volume fraction
q	impingement angle of a jet with the plane of symmetry
r_j	jet density
s	liquid jet surface tension
s_N	deviation of the normalized diameter

1. Introduction and Backgroung

Liquid propellant rocket engines are an important component of the space program due to their relatively high specific impulse, capability to be randomly throttled, stopped, and restarted, reusability, and the capability to responsively control operating conditions during use [1]. While all of these characteristics may not be utilized in each engine, collectively they have made liquid propellant rocket engines the propulsion system of choice for many applications such as the Space Shuttle Main Engine (SSME), the Apollo and Saturn V programs [2], and most satellite attitude control systems. Additionally, as the space program matures, areas such as global communication networks and environmental monitoring of the earth's ecosystem are becoming dependent on the ability to deploy complex earth orbiting satellites; therefore, the need for liquid propellant rocket engines and thrusters will continue. However, the funding available for the large scale testing of rocket propulsion systems, which historically has been the primary means of development and design, is steadily reducing. Consequently, there is a significant need to conduct basic research that will lead to a thorough, fundamental understanding of the mechanisms prevalent in liquid rocket propulsion. Combined with the experience of previous development programs, the information gained through basic research will permit new space launch systems to be designed more effectively up front, thus reducing the quantity of large scale tests needed, and therefore the cost required to produce a reliable engine.

Two of the most important aspects affecting the performance and stability of liquid propellant rocket engines are the atomization and mixing of the fuel and oxidant that are injected into the combustion chamber. Impinging jet injectors are one of the most popular designs due to their inherent simplicity, low fabrication costs, and good mixing characteristics [3]. However, a poorly designed injector can lead to combustion instabilities characterized by sustained pressure oscillations with frequencies from several hundred to over one thousand Hertz. High frequency instabilities can lead to the overheat of the injector surface and combustion chamber wall, the loss of combustion and performance predictability, and under a worst case scenario, loss of the vehicle. Experimental studies of the spray characteristics of impinging jets began in the early 1950's with

the work of Heidmann and Humphrey [4,5]. They examined the instability of the liquid sheet formed from impinging jets, and the resulting disintegration of the sheet into intermittent waves of droplets [4]. Their work extended to a full investigation of the effect of the jet velocity (1.5 to 30 m/s), impingement angle (30° to 100°), pre impingement jet length (10 to 60 jet diameters), jet diameter (0.635 to 1.3 mm), fluid surface tension, and viscosity on the resulting spray [5]. Four different atomization regimes were identified as a function of increasing jet velocity: closed rim, periodic drop, open rim, and fully developed. The fully developed regime is most relevant to liquid rocket injectors, and it is therefore the case examined in this article.

In the late 1950s and early 1960s, research efforts were focused on obtaining the spatial characteristics of impinging jet sprays. Ingebo [6] quantified the drop-size distribution for heptane jets impinging at 90°, and obtained an empirical expression relating the orifice diameter, jet velocity, and the velocity difference between the jet and surrounding air stream to the volume mean diameter. Heidmann and Foster [7] performed an experimental analysis of water jets impinging at 90°, and they determined that the velocity of drops in a fully developed spray was maximum along the spray axis and minimum normal to the spray axis. Additionally, they observed that 50% of the total mass of the spray was contained within an envelope ±20° of the spray axis, and that the largest drops, on the order of the jet diameter, were also located along the spray axis. Later Heidmann and Foster [8] included the effect of impingement angle on the spatial characteristics of the water jets. The drop-size distributions were noted as having a bimodal shape.

The effects of the flow condition of impinging liquid jets on the mechanism of spray disintegration were studied by Dombrowski and Hooper [9], and Huang [10]. Dombrowski and Hooper [9] determined that in addition to the aerodynamic instability factor resulting from the non-equilibrium condition between the surface tension and aerodynamic forces, the impingement of two obliquely colliding jets causes a hydrodynamic instability in the form of impact waves when the Weber number ($We_j=r_jD_jV_j^2\sin^2q/s$) of each jet is above a critical value ($66<We_{crit}<165$). Upon the transition to turbulent flow and for Weber numbers beyond the critical value, the hydrodynamic impact waves dominate the entire spray region. Huang [10] investigated the breakup mechanism

of an axisymmetric liquid sheet formed by the impingement of two coaxial water jets. Huang also identified hydrodynamic waves as the governing factor for sheet disintegration at increased Weber numbers.

Experimental research over the last fifteen years has been highlighted by the utilization of various non intrusive optical techniques. Lourme [11] measured the drop-size distribution of an impinging jet spray by employing the light scattering based Malvern size analyzer. Santoro et al. [12] examined the atomization of impinging jets on the basis of the flow condition of the jet and the injector geometric parameters through the use of a Phase Doppler Particle Analyzer (PDPA). Their experimental results were compared with analytical linear stability models. Similarly, Vassallo [13] used PDPA to study impinging jets. The advantage of the PDPA system over previous optical methods is the quantity of information obtainable. Specifically, the PDPA system is capable of acquiring diameter, velocity, number density, and volume flux information simultaneously at large sample rates. However, the PDPA system is still only capable of obtaining data at a discrete location within a spray containing spherical liquid elements.

Kuo et al. [14] focused on the characteristics of the dynamic interaction between two impinging jets in the region near the injector. The visualization of the inner jet breakup and mixing processes, as well as the outer spray boundary configurations of water jets at various velocities (3.5 to 32.6 m/s) and impingement angles (15° to 75°), was made by pulse laser illuminated instantaneous and time averaged photography. When the jet Reynolds number was beyond a critical value, the nature of the spray changed slightly from that described by Heidmann [5] as the fully developed regime. This suggested a new regime characterized by the break down of the periodic wave nature observed up to this point. The absence of a well defined wave breakup pattern is believed to be caused by increased turbulence intensity.

More recently, Kang et al. [15] utilized double pulse, two reference beam holography to investigate the disintegration of the sheet formed by two low speed impinging jets. Particle velocity and size measurements were taken at the periphery of the sheet, and the shape and size of the sheet were measured. Experimental results were marked by large size variations locally, and

the particles were largely non spherical in shape. Existing theoretical models assumed a monodispersed drop distribution at all angular locations, and therefore, did not accurately predict drop sizes when compared with the experimental data. In addition to Kang's work, researchers at Phillips Laboratory [16] have recently conducted investigations of the mixing mechanisms of impinging jets. Results indicate that a majority of the mass of either jet can be delivered to the opposite side of the spray. This phenomenon is potentially explained by the helical structure of the jets prior to impingement that was also recently observed by Ashgriz et al. [16].

The majority of the previous work outlined thus far has focused on the atomization characteristics of impinging jets at atmospheric temperatures and pressures. However, typical values experienced within the combustion chambers of large liquid propellant rocket engines range between temperatures of 3000 to 3500 K, and pressures of 15 to 25 MPa [1]. It is therefore expected that the atomization characteristics will change as the ambient conditions are increased towards actual rocket operating conditions; thus, the characteristics of impinging jet sprays at elevated temperatures and pressures must be investigated. To this end, this research examines the effect of temperature on the drop-size and velocity distributions at various regions within impinging jet sprays; and the dependence of the overall qualitative nature of the spray pattern with temperature is evaluated. The experimental method employed is a novel, double pulse holographic technique. A brief description of the holographic system is provided, including a discussion of its primary advantages. Experimental diameter data, represented by the universal root-normal cumulative volume distribution, are then presented for all regions of fully developed impinging jet sprays at both atmospheric and elevated temperatures. In addition, velocity measurements are presented for the aqueous glycerol solution and ethanol. For both the diameter and velocity data, the dense region of the spray near the impingement point, which is difficult to study with more conventional methods, is also included in the results.

2. Experimental Setup and Procedure

2.1 Impinging jet apparatus and high temperature chamber

The test fluid is contained within a reservoir pressurized with nitrogen gas. The liquid is forced from the reservoir, through a ball valve that serves as an on/off device, and through 6.35 mm tubing to a variable area flow meter. After exiting the meter, the flow is split into two identical branches, with a pressure gauge present on each branch to ensure that the flow is equally divided. Each of the two branches feeds one of the jets. The jet injectors are precision bore 0.79 mm stainless steel tubes with a length of 20.3 cm (L/D_j=256). The large length to diameter ratio ensures that the flow is fully developed upon exiting the injector. To provide support for the small diameter injector tubes, they are concentricly housed in 6.35 mm diameter stainless steel tubes that are in turn connected to the liquid feed lines. The injectors are inserted into the high temperature chamber of Figure 1 with an impingement angle (2q) of 90°, and a pre impingement length of 12.5 mm. The injector housings are fixed to the chamber by a Swagelok™ tube connector.

As shown in the Figure 1, the high temperature chamber is made of a 15.24 cm ID, 25.4 cm long stainless steel pipe with a 0.95 cm wall thickness. Optical windows of five cm in diameter are installed on the two sides of the chamber cover. Each window is placed eccentric relative to the center of the cover so that the observation position can be changed by rotating the cover. A total of six 500 W electrical cartridge heaters are installed on the bottom side of the cover as the heat source. Cylindrical brass fins are installed on each heater to enhance the heat transfer. In addition, a layer of fiberglass insulation was installed on the outside of the chamber to reduce heat loss and insure temperature uniformity. The chamber can be pressurized to one MPa, and the temperature within the chamber can be raised to 300°C within 30 minutes.

2.2 Double pulse two reference beam holographic system

The impinging jet apparatus was placed in the optical system within the path of the object beam, as shown schematically in Figure 2. As a novel technique, the system is able to record two distinct holograms separated temporally by a specified time interval on one film, and then

reconstruct them separately. The interval between exposures and the exposure duration were 100 ms and 30 ns respectively. The feature which allows two images to be recorded on the same film is that the two separate laser pulses are split into two different reference beams polarized in planes normal to each other. To this end, a double pulse ruby laser that generates a 694 nm wavelength, vertically polarized laser beam with an energy output of 2 J was utilized as the light source. A Pockels cell, driven by the high voltage pulse generator and synchronized with the laser, is used to change the polarization direction of the first pulse of the laser beam. The polarizing beam splitter reflects the incident beam with vertical polarization components, while permitting the light with horizontal polarization components to pass undeviated. In this manner, the first laser pulse, whose polarization direction is changed by the Pockels cell to the horizontal plane, will pass through the beam splitter to form the first reference beam. The Pockels cell is not activated for the second pulse, therefore, it retains its vertical polarization direction and is consequently reflected by the polarizing beam splitter to form the second reference beam as shown in Figure 2. The object beam for both pulses is expanded and passed through the optical windows of the high temperature chamber. The two combinations of reference and object beams, each pair polarized in planes normal with respect to the other pair, record two distinct holographic images separated by a known time interval on one film.

The double pulse holographic method has three distinct advantages. The first advantage is the ability to analyze dense spray regions, such as near the impingement point. This feature is a result of the very short exposure times that effectively freeze the motion of the spray elements, and the large depth of field that is characteristic of holographic methods. Furthermore, the small interval between exposures enables velocity measurements to be made due to the small particle displacements that occur between exposures. The second advantage is that non spherical shapes can effectively be analyzed. Again, it is the short duration between exposures that allows the same spray particle to be identified in each of the two holographic images. The final advantage is the ability to obtain both velocity and size measurements for an entire spray region simultaneously.

2.3 Experimental methods

First, the cartridge heaters were activated to increase the chamber temperature, while the pressure remained constant at atmospheric pressure due to a drain at the bottom of the vessel. The chamber temperature was monitored by an Omega three mm OD, metal sheathed, K type thermocouple mounted through the chamber wall at a location 90° from the injector tubes such that the measurement junction was at the center of the chamber. The temperature was increased slightly beyond the desired value, and then the cartridge heaters were turned off. The chamber was then allowed to cool to the desired temperature. Since the chamber was well insulated, the cooling process was slow and the chamber was effectively isothermal during the short duration that the spray was activated. Once the desired temperature was obtained, the valve on the liquid supply line of the jets was opened and the impinging jet spray formed within the chamber, with the liquid exiting the chamber through a drain located well downstream of the spray. The pulsed ruby laser, synchronized with the high voltage pulse generator, was fired immediately after the spray developed. The steady state chamber temperature was measured at the instant between the first and second pulse via a HP 9122 computer and 3852A data acquisition system synchronized with the pulse generator. The timing sequence was monitored by a HP 54601 oscilloscope and the output is illustrated graphically in Figure 3. Furthermore, repeatability and consistency of the observed experimental trends were verified by conducting identical trials separated by one month and obtaining the same trends.

The impinging jet spray was divided into an upper and a lower region for the various measurements. The upper region boundaries were defined by a 30 mm radius originating at the impingement point and extending from the spray centerline to an azimuthal angle of ±100°. The lower region consisted of the area within an azimuthal angle of ±10° and a radius of 50 mm to 80 mm. The measurements were divided spatially in this manner due to the eccentric location of the chamber window as described earlier, and due to the significant difference in the value of the drop sizes within the two zones.

Holographic images of the impinging jet sprays for each of the three test fluids were acquired at temperatures ranging from room temperature to 250°C. An experimental run consisted of injecting the spray into the test chamber and recording the separate images from the two laser pulses on a single holographic plate. Minimally, three runs were conducted for each combination of temperature, test fluid, and measurement region. The drop size measurements obtained from all of the runs at each distinct operating condition were combined, yielding sample sizes of approximately 5,500 drops for each case.

2.4 Image Reconstruction and Processing

A schematic of the image reconstruction system is shown in Figure 2. A Kodak 1000 HRC EKTAPRO high speed motion analyzer, with a maximum acquisition rate of 1000 frames/second, was placed behind the holographic film to record the reconstructed images. Traditionally, the holograms recorded by the pulsed ruby laser are reconstructed by a continuous output He-Ne laser. However, this reconstruction method is not ideally suitable in this application because the differences in wavelength between the He-Ne laser and the ruby laser cause the two images reconstructed by the He-Ne laser to be offset from each other. Thus, the two images lose their absolute reference frame, and therefore, velocity measurements become tedious. To rectify this problem, the ruby laser was used to reconstruct the holograms and eliminate the optical distortion. The two holograms reconstructed by the pulsed laser were recorded separately by the high speed camera. The images were then transferred from the Kodak camera to a personal computer via a frame grabber board.

The spray image analysis was performed using the Image Analyst software package from Automatix, Inc. Spray particles were identified from the background and noise by the image processing system using a grayscale threshold value. The drop diameters were calculated by equating the measured cross-sectional area to the that of a circular drop of equivalent area. The velocity measurements were made by measuring the change in location of the centroid of a single droplet between the two images. The two images both share the same absolute reference frame as

a result of using the pulsed ruby laser as the reconstruction device. Therefore, the displacement of the particle is absolute and the corresponding velocity is calculated as the ratio of the displacement to the time interval between the pulses. Thus, the two reference beam, two pulse holographic system is capable of acquiring both the temporal and spatial characteristics of the entire spray simultaneously.

The mean velocity of the jets was 12.5 m/s, therefore, the pulse interval was set at 100 ms to achieve approximately a 1 mm displacement of the spray elements. Particular attention must be given to the pulse interval when analyzing the velocity field in the dense region of the spray to ensure that the same particle can be identified in each of the two images. If the pulse interval is too long, the displacement of the drops is too large and identification is difficult. Though the identification process is currently manual, it is made straightforward by continuously alternating the displayed image on the computer. This provides a type of computer animation, which makes it easier to identify specific droplets in each of the two exposures. To explain this method, an analogy is drawn with a frog catching insects. The frog has very little chance of finding insects which are at rest on the plats, while an insect in flight is an easy target. From the analogy and experience, it is known that particle recognition is easier to perform with dynamic rather than static image display.

3. Results and Discussion

3.1 Qualitative Behavior

Images of the reconstructed holograms for the water, glycerol (59% weight solution with water), and ethanol sprays are shown in Figures 4, 5, and 6 respectively. Images at both atmospheric conditions and high temperatures are given for each test fluid. The mean jet velocity is 12.5 m/s, the injector tube diameter is 0.8 mm, and the impingement angle (2q) is 90° for all cases. The jet Weber numbers under the given conditions are 870, 1140, and 2250 for water, glycerol, and ethanol respectively at 25°C. Consistent with the observations of other investigators, a fan-shaped liquid sheet is formed around the impingement point due to the oblique collision of the high

speed jets. The breakup of the spray is in the fully developed regime, thus, the resulting spray is dominated by circumferentially aligned, intermittent waves of ligaments detaching from the sheet near the impingement point. For the ethanol and water sprays, the ligaments break down into groups of droplets shortly after detaching from the sheet.

A comparison between the atmospheric and high temperature sprays for each of the test fluids indicates that the same breakup mechanisms are present due to the consistent wave pattern observed. However, quantitative characteristics such as the diameter of the droplets and the distance at which the ligaments break up begin to change. In Figure 4b for example, the ligaments formed by the impinging water jets are thinner, and they break into droplets earlier than the ligaments observed in Figure 4a at atmospheric conditions. This is an expected result considering that the viscosity of air at atmospheric pressure increases with temperature, whereas the spray fluid viscosity decreases with temperature. Therefore, the aerodynamic instabilities that cause the ligaments to break up into drops will grow faster.

For the aqueous glycerol solution of Figure 5, the appearance of the spray is changed more dramatically with temperature than that of water. This is in part due to the behavior of the viscosity of glycerol. For an increase of temperature from 25°C to 50°C, the viscosity of pure glycerol decreases by 84%, compared with a decrease of only 38% for water [17]. Panels two and three of Figure 5b indicate the presence of a small number of droplets, which were completely absent in the atmospheric temperature conditions. Furthermore, the wave pattern becomes less distinct at higher temperatures, although it is still clearly present.

Figure 6 illustrates the effect of increasing temperature on ethanol sprays. The differences are similar in nature with the water and glycerol cases. Namely, the intermittent wave nature becomes less distinct, the ligaments begin to break into droplets earlier, and the fundamental shape of the resulting spray is retained. Furthermore, the majority of the mass is contained within a zone approximately 20° each side of the spray centerline in both the atmospheric and high temperature cases. This again supports the conclusion that the same fundamental spray atomization

mechanisms are present under both conditions, with only a change in the magnitude of the resulting structures distinguishing the two different cases.

3.2 Quantitative Drop-Size and Velocity Results

The cumulative volume fraction corresponding to the measured drop diameters was determined for each combination of chamber temperature, spray fluid, and measurement region. The sample size for each case was at least 5,500 droplets, ensuring an accuracy within 5% for the representative diameters. Three of the standard cumulative volume distribution functions, the universal root-normal, the Rosin-Rammler, and the modified Rosin-Rammler, were fit to the data. The form of the universal root-normal distribution proposed by Simmons [18] is

$$Q(D_N) = \frac{1}{2}\left(1.0 + erf\left(\frac{D_N - \overline{D_N}}{\sqrt{2}\sigma_N}\right)\right) \qquad (1)$$

where Q is the cumulative volume fraction, D_N is the square root of the drop diameter normalized by the mass median diameter ($D_{0.5}$), and s_N is the deviation of D_N The form of the Rosin-Rammler and modified Rosin-Rammler distributions are discussed in detail by Lefebvre [19].

The experimental data for the top region of the ethanol spray at 25°C and the bottom region of the water spray at 250°C are compared to the various distribution functions in Figures 7a and 7b respectively. The deviation of the distribution functions from the experimental data in Figure 7a was largest for the cases examined, while the results of Figure 7b were typical. The universal root-normal distribution provided the best fit to the data over all cases examined. The deviation of the data from the distribution functions was greatest between a volume fraction of 0.75 and 0.95 for each of the cases. This phenomenon is potentially explained by the bimodal characteristics of impinging jet sprays that Foster et al. [8] observed. Despite the slight deviation, the universal root-normal distribution still adequately represented the characteristics of the drop size distributions.

The universal root-normal distributions for the upper and lower regions of the ethanol and water impinging jet sprays are shown in Figures 8a and 8b respectively for various temperatures. Generally, as the ambient temperature is increased, the large droplets become smaller and the drop distribution is more uniform. Two mechanisms resulting from the increased ambient temperature are responsible for the smaller droplet diameters. First, as stated earlier, increasing the temperature increases the viscosity of the air and decreases the viscosity of the spray fluid. Thus, the aerodynamic instabilities that cause the primary atomization of the larger spray structures will grow faster, and therefore, the spray will atomize earlier as observed qualitatively in Figures 4 through 6. Furthermore, the size of the droplets that form from the ligaments tends to decrease with viscosity. Simultaneously, the heat transfer to the droplets is enhanced by the increased surface area, and thus evaporation of droplet mass becomes the second mechanism reducing the droplet diameters. The data were not corrected for the evaporation of smaller droplets; therefore, the distributions do not change a great deal for the smaller diameter sizes as the larger droplets decrease in size and fill the void created by vaporization of the smallest droplets.

Figures 9a and 9b are plots of the Sauter mean diameter and the mass median diameter in the upper and lower regions for ethanol and water respectively. Each data point is a representative diameter taken from a sample size of at least 5,500 droplets. Both the Sauter and mass median diameters decrease with increasing temperature until it is well beyond the boiling point of each fluid. At a temperature of approximately 80° beyond the boiling point of ethanol and 150° beyond the boiling point of water, both the Sauter mean diameter and the mass mean diameter for the upper region increase with temperature because the diameter of the smaller droplets is affected to a greater degree by evaporation than that of the larger droplets. The Sauter mean and mass median diameters both are greatly influenced by the larger droplets. Therefore, while individual droplet sizes are steadily decreasing with temperature, the representative diameters increase over a short temperature span as a result of the disappearance of the smaller droplets. Eventually, the representative diameters begin decreasing with temperature again, for the ethanol case. Similarly, it is expected that for temperatures beyond those examined in the current work, the representative

diameters for water in the upper region will also begin decreasing with temperature again. This is supported by the water data in the lower region, which exhibits the increasing diameter trend earlier than in the top region because the drops have had more time to heat up. The counter-intuitive trend of representative diameters increasing with temperature illustrates the importance of presenting both a representative diameter and a distribution parameter when analyzing sprays.

The velocity of a droplet was determined as the ratio of the absolute displacement of the centroid divided by the time interval between exposures. Figure 6 highlights the apparent difficulty in analyzing the velocity of dense sprays, that is how to identify the same particles from one image to the next. This was discussed earlier, but it should be noted again that without using intrusive methods, it would be extremely difficult to measure the velocity within this region due to the density and non-uniformity of the spray structures. Figure 10a is the velocity vector field, and Figure 10b is the velocity distribution as a function of the azimuthal angle for the dense region of an ethanol spray at 251°C. The velocity distribution indicates that the average velocity of the particles near the centerline of the spray is approximately equal to the mean velocity of the jets. As the azimuthal angle increases, the average velocity of the droplets decreases until an angle of 80° and beyond, where the average particle velocity is approximately half that of the mean jet velocity. This corresponds to the data collected by Heidmann and Foster [7]. In addition, the direction of the droplet velocities tends to correspond to the azimuthal angle.

Figure 11 shows the velocity vector field for the bottom region of a glycerol spray at a temperature of 200°C. At this location, the droplet density is considerably less and the shapes are more spherical. Therefore, the droplets are easier to identify and the velocity determination is simplified. The velocity direction at this location is almost entirely downward and the magnitude of the average velocity has been reduced to approximately 65% of the original jet velocity by aerodynamic drag. Currently, the analysis of the images is manual, however, the automation in the regions of lower droplet density such as Figure 11 is forthcoming. Within the dense area of the spray near the impingement point, the recognition of identical structures is not as straightforward

and it therefore requires a great deal of human judgment and insight. The development of pattern recognition algorithms involves significant complexity.

3.3 Error Analysis

There were two primary sources of systematic errors present in the measurement of the droplet diameters: the uncertainty incurred from the calibration of the image analysis system, and the uncertainty of the measured droplet pixel diameters resulting from the selection of a grayscale threshold value. First, the calibration of the image analysis system entailed determining a micron to pixel ratio. This was established by measuring the distance between two lines of a 5 mm by 5 mm calibration grid. The uncertainty in the measurement was one pixel at each of the end points. Therefore, the total error resulting from the calibration of the system for the magnification used was ±0.29 mm/pixel, and for a micron to pixel ratio of 27, this corresponds to a relative error of approximately 1%. The second source of error was the selection of a proper grayscale threshold value. The threshold value determines the location of the droplet boundaries by distinguishing the grayscale intensity of the droplet from the background and noise. To rigorously determine the uncertainty in the droplet diameter measurements, an investigation of the diameter sensitivity to the threshold value was performed. Since the droplet diameter in pixels was determined by the image analysis software by equating the area of the droplet to the area of a circle, an ideal threshold value that would accurately determine the area assuming a standard background grayscale value was determined. Then, the threshold was varied in intensity around the ideal value. The diameter of the droplets were measured at each of the new threshold values. The variation over the entire range of threshold values corresponds to the uncertainty associated with this parameter. As expected, the uncertainty increased as the droplet size decreased. For example, the relative error resulting from the selection of a proper threshold value for a 115 mm droplet was measured to be 17%, whereas for 200 mm droplet, the error was found to be only 4.5%. Since the cumulative volume distribution, Sauter mean diameter, and mass median diameter are influenced primarily by droplet sizes over 200 mm, the uncertainty for the representative diameters and drop-size distributions

resulting from the selection of a proper grayscale threshold value was determined to be 4.5%. Finally, because the diameter values are determined by the multiplication of the measured pixel length by the calibrated micron to pixel ratio, the total relative error is found to be the square root of the sum of the squares of each of the individual sources of error. Therefore, the total uncertainty for the diameter data was determined to be approximately 5%.

For the velocity measurements, the sources of uncertainty were the calibration error and the selection of a proper discrete point that accurately defines the particle displacement. As discussed above, the error attributed to the calibration of the system was determined to be approximately 1%. The error in measuring the displacement is larger. The non spherical particles may have a rotational velocity component that will affect the value of the measured displacement depending on which point of the particle it is measured from. This problem is compounded by the difficulty in determining the proper discrete location, such as the centroid of the spherical droplets, due to the non symmetric shapes. However, a sensitivity investigation of the velocity measurement error can be performed by measuring the displacement of several discrete points of a particle. The variation in the resulting velocities calculated from different points corresponds to the uncertainty. Thus, the velocity measurement uncertainty was determined to be approximately 15% for the combined calibration and displacement measurement errors.

4. References

1. G. P. Sutton, *Rocket Propulsion Elements*, 6th ed., John Wiley and Sons, New York, NY, 1992.
2. J. C. Oefelein and V. Yang, Comprehensive Review of Liquid-Propellant Combustion Instabilities in F-1 Engines, *J. Propulsion* , vol. 9, pp. 657-677, 1993.
3. W. E. Anderson, H. M. Ryan, S. Pal, and R. J. Santoro, Fundamental Studies of Impinging Liquid Jets, AIAA paper 92-0458, 30th Aerospace Sciences Meeting, Reno, NV, Jan. 1992.
4. M. F. Heidmann and J. C. Humphrey, Fluctuations In a Spray Formed By Two Impinging Jets, National Advisory Committee for Aeronautics Rept., TN2349, 1951.
5. M. F. Heidmann, R. J. Priem, and J. C. Humphrey, A Study of Sprays Formed by Two Impinging Jets, National Advisory Committee for Aeronautics Rept., TN3835, 1957.
6. R. D. Ingebo, Drop-Size Distributions for Impinging-Jet Breakup in Airstreams Simulating the Velocity Conditions In Rocket Combustors, National Advisory Committee for Aeronautics Rept., TN4222, 1958.
7. M. F. Heidmann, H. H. Foster, Spatial Characteristics of Water Spray Formed By Two Impinging Jets at Several Jet Velocities in Quiescent Air, National Aeronautics and Space Administration Rept., TN D-301, 1960.
8. M. F. Heidmann and H. H. Foster, Effect of Impingement Angle on Drop-Size Distribution and Spray Pattern of Two Impinging Water Jets, National Aeronautics and Space Administration Rept., TN D-872, 1961.
9. N. Dombrowski and P. C. Hooper, A Study of the Sprays Formed By Impinging Jets in Laminar and Turbulent Flow, *J. Fluid Mech.*, vol. 18, pt. 3, pp. 392-400, 1963.
10. J. C. P. Huang, The Breakup of Axisymmetric Liquid Sheets, *J. Fluid Mech*, vol. 43, pt. 2, pp. 305-319, 1970.

11. D. Lourme, D. Schmitt, and F. Brault, Experimental Characterization of the Spray Originating From an Impinging-Jet Injector in a Liquid Rocket Engine, *Acta Astronautica*, vol. 11, pp. 469-482, 1984.

12. H. M. Ryan, W. E. Anderson, S. Pal, and R. J. Santoro, Atomization Characteristics of Impinging Liquid Jets, *J. Propulsion*, vol. 11, pp. 135-145, 1995.

13. P. Vassallo, *Spray Characterization of Impinging Water Jets Using a Phase Doppler Particle Analyzer*, M.S. thesis, University of New York at Buffalo, Buffalo, NY, 1990.

14. K. K. Kuo, F. B. Cheung, R. D. Woodward, M. C. Kline, and R. L. Burch, Experimental Observation of Dense Spray and Mixing Impinging Jets, National Aeronautics and Space Administration Rept., CR-190113, pp. 46-64, 1992.

15. B. S. Kang, Y. B. Shen, and D. Poulikakos, Holography Experiments in the Breakup Region of a Liquid Sheet Formed by Two Impinging Jets, *Atomization and Sprays,* vol. 5, pp. 387-402, 1995.

16. N. Ashgriz, D. G. Talley, and W. Brockelhurst, On the Mixing Mechanisms of a Pair of Impinging Jets, AIAA paper 95-2421, 31st AIAA/ASME/SAE/ASEE Joint Propulsion Conference, San Diego, CA, July 1995.

17. D. R. Lide, Ed., *Handbook of Chemistry and Physics*, 76th ed., CRC Press, Inc., Boca Raton, FL, 1995.

18. H. C. Simmons, The Correlation of Drop-Size Distributions in Fuel Nozzle Sprays, *Journal of Engineering for Power*, vol. 99, pp. 309-319, 1977.

19. A. H. Lefebvre, Atomization and Sprays, Hemisphere Publishing Corporation, N.Y., 1989.

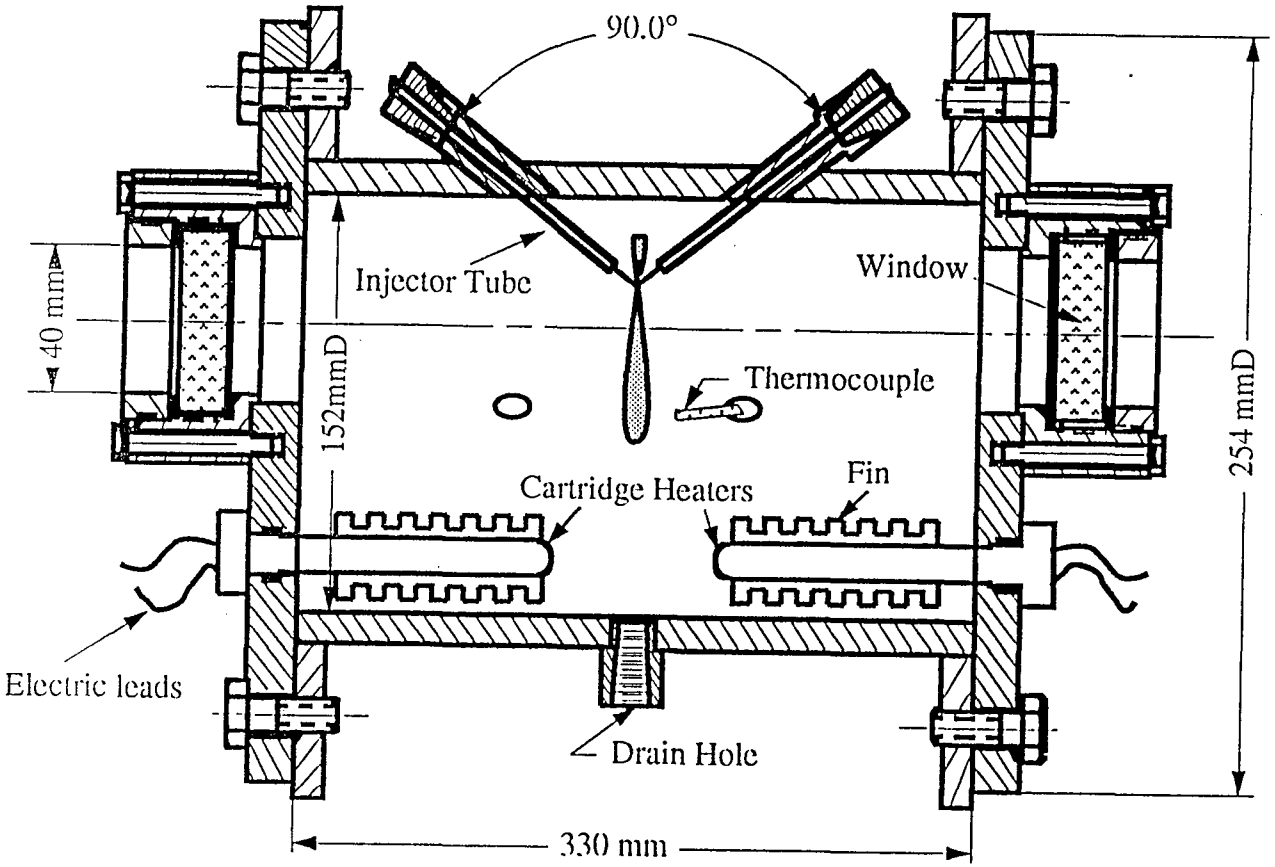

Figure 1 High temperature chamber for impinging jet experimental setup.

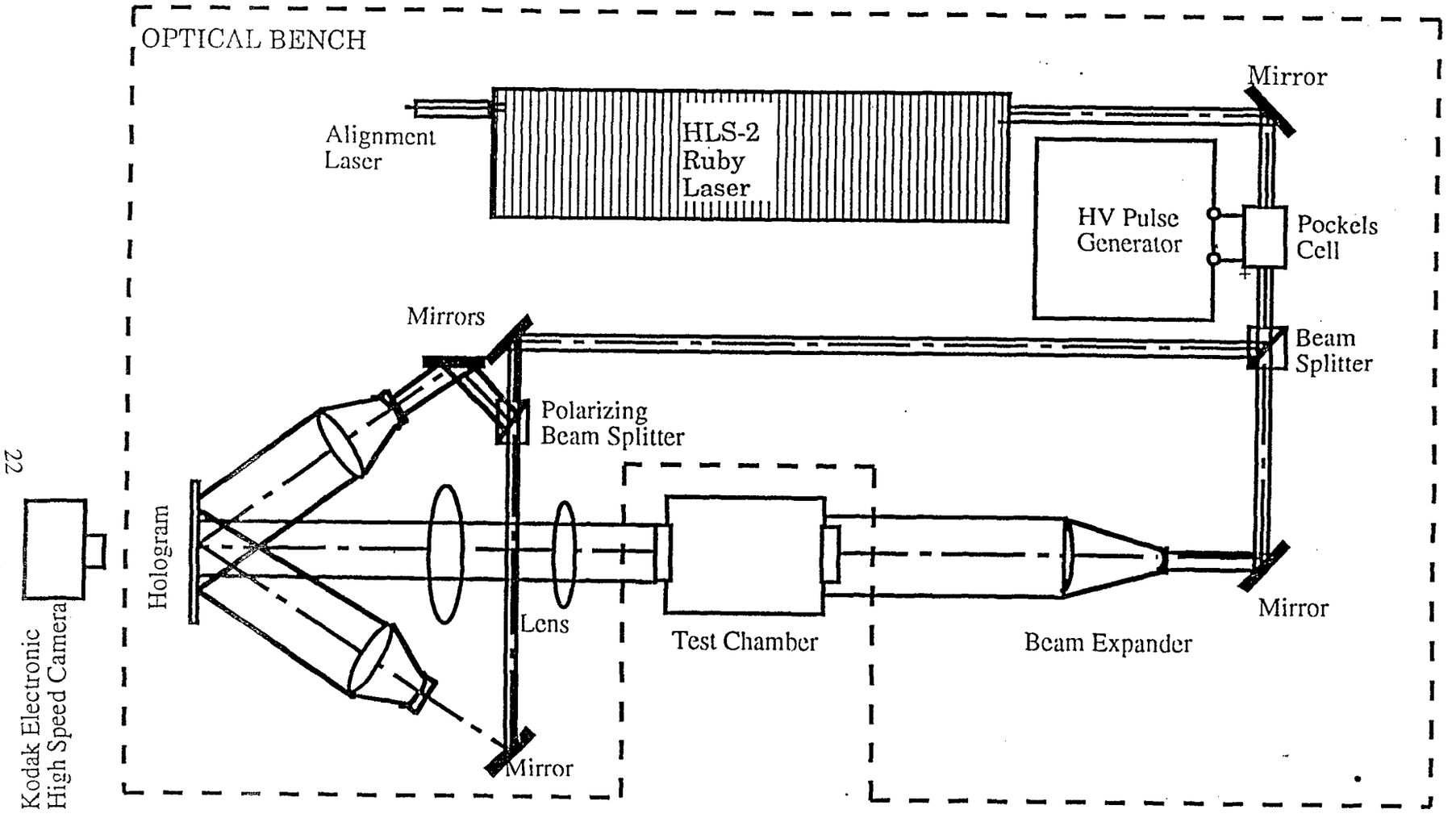

Figure 2 Schematic of the double pulse holography optical setup.

Figure 2

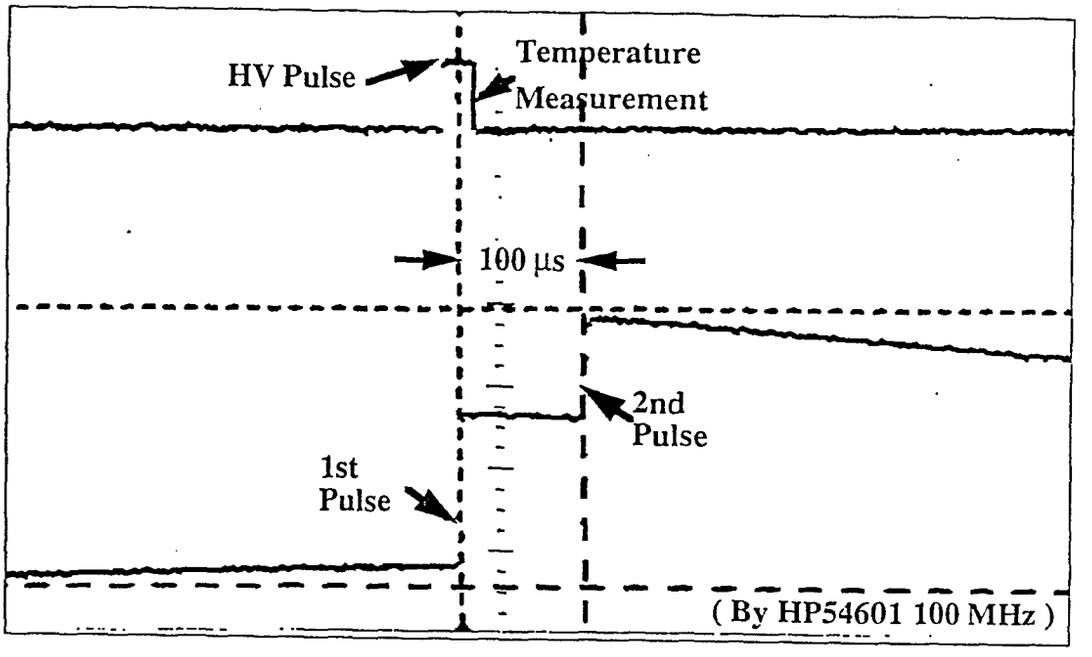

Figure 3 Double pulse holography timing diagram for high temperature conditions.

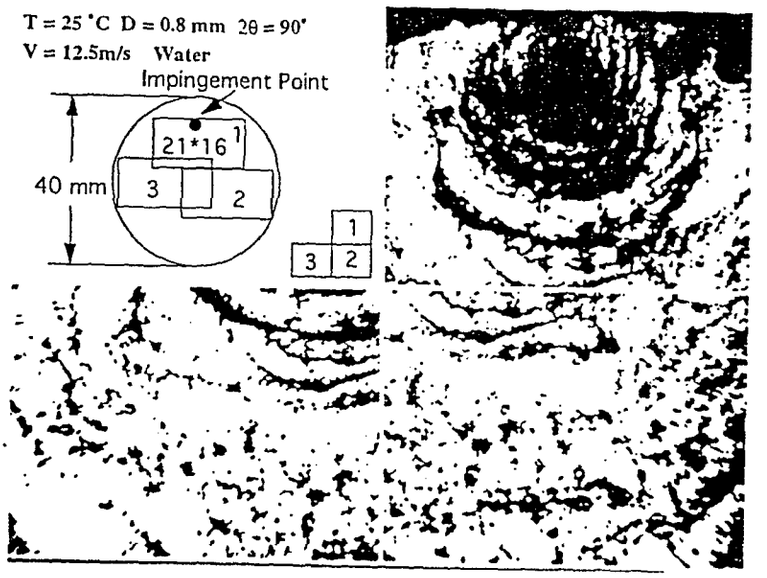

(a)

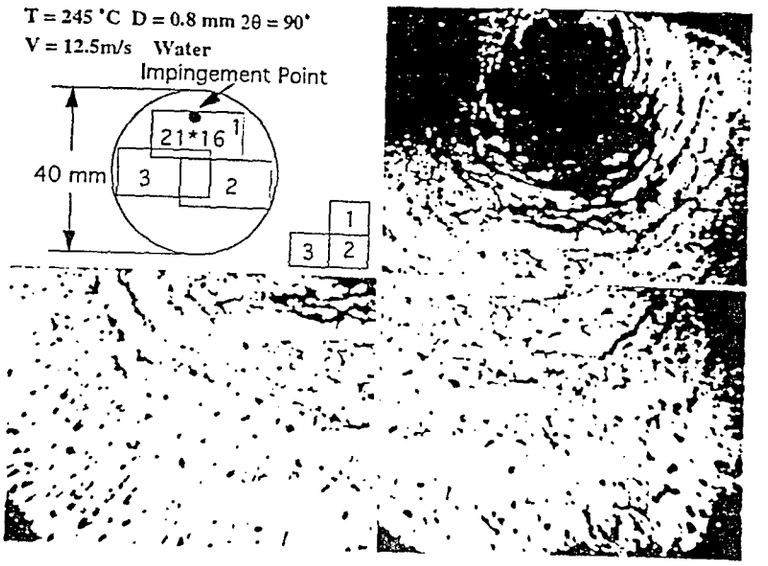

(b)

Figure 4 Images of a water impinging jet spray hologram at a temperature of (a) 25°C and (b) 245°C.

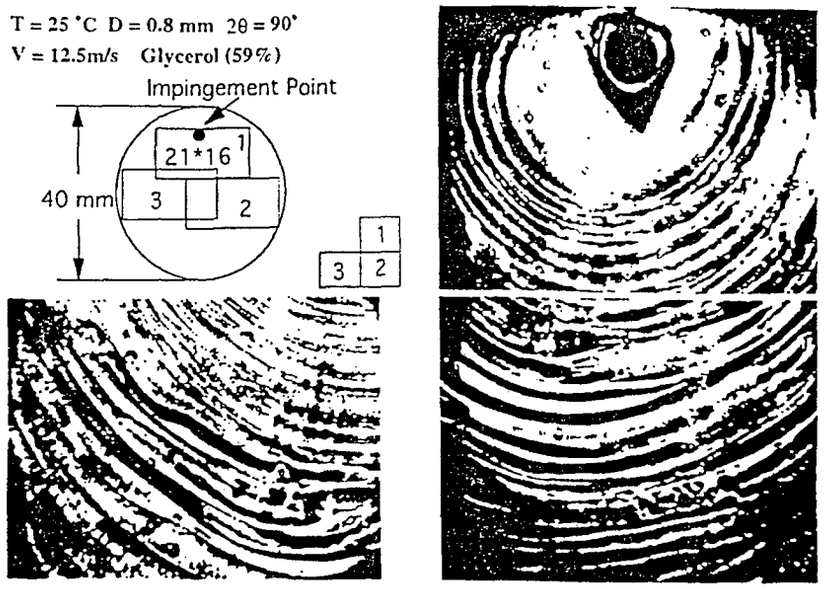

(a)

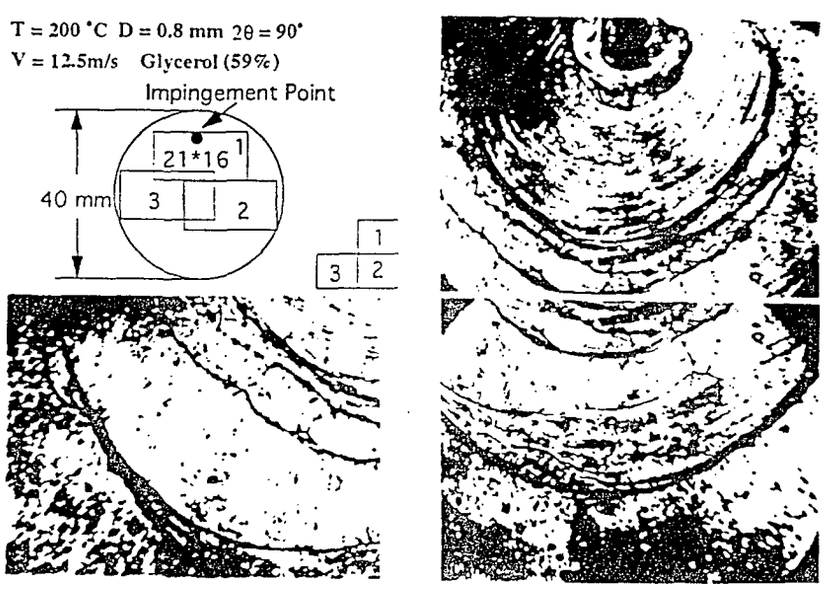

(b)

Figure 5 Images of an aqueous glycerol solution impinging jet spray hologram at an ambient temperature of (a) 25°C and (b) 200°C.

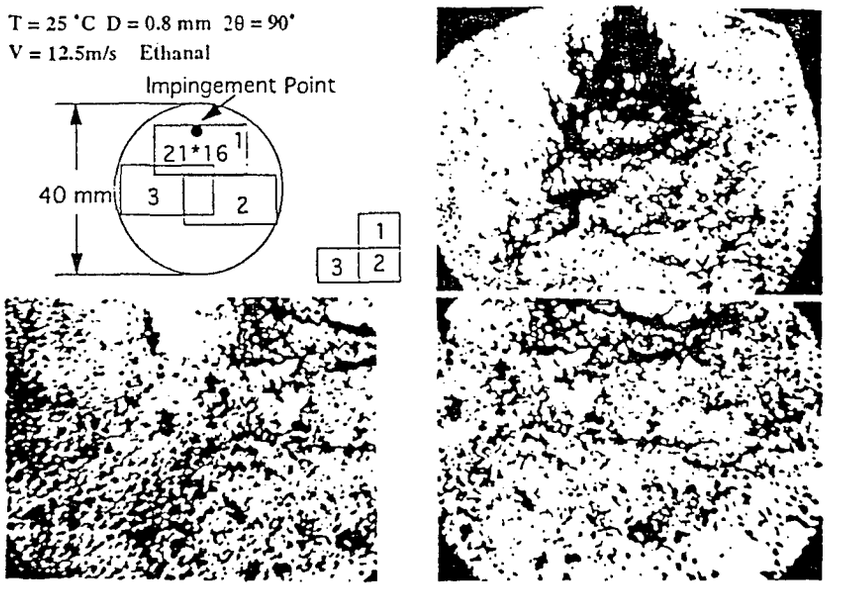

(a)

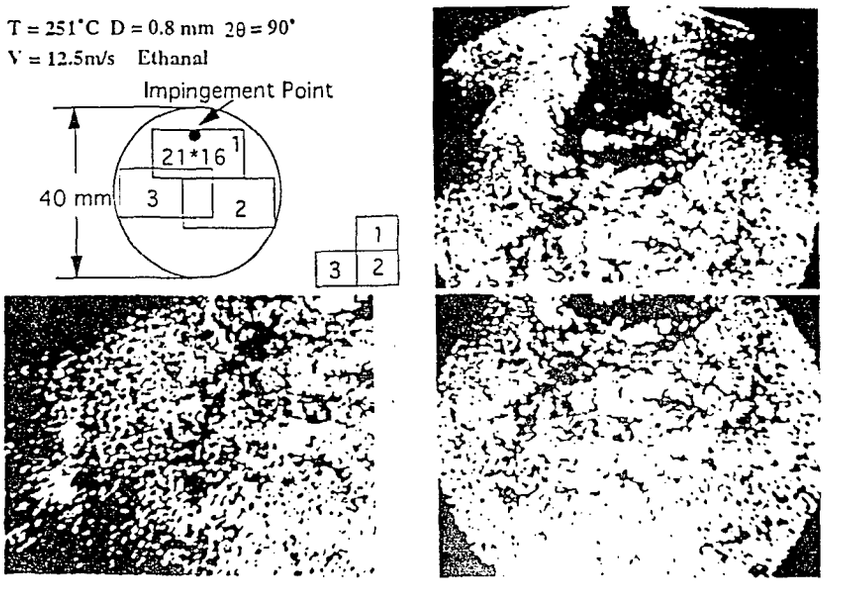

(b)

Figure 6 Images of an ethanol impinging jet spray hologram at an ambient temperature of (a) 25^{o}C and (b) 251^{o}C.

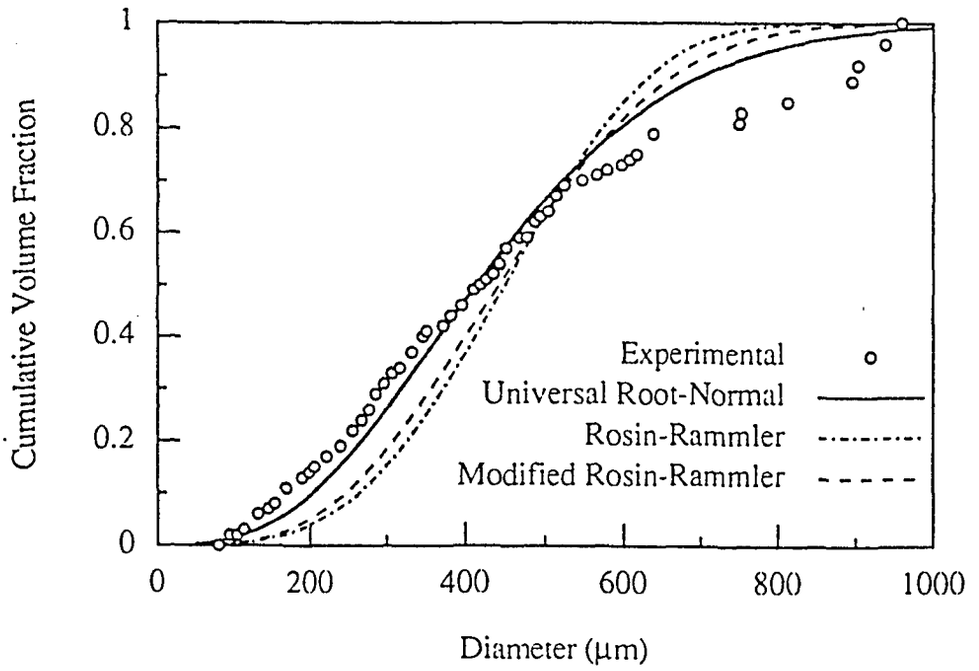

(a)

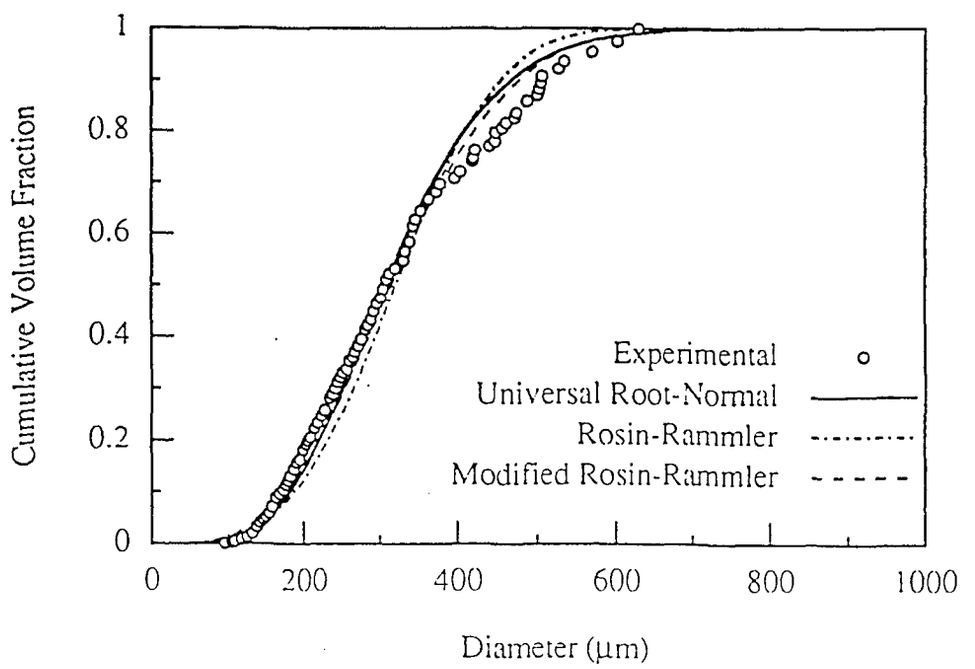

(b)

Figure 7. Comparison of the experimental cumulative volume distribution with the universal root-normal, Rosin-Rammler, and modified Rosin-Rammler distributions for (a) the upper region of an ethanol spray at 25°C and (b) the lower region of a water spray at 250°C.

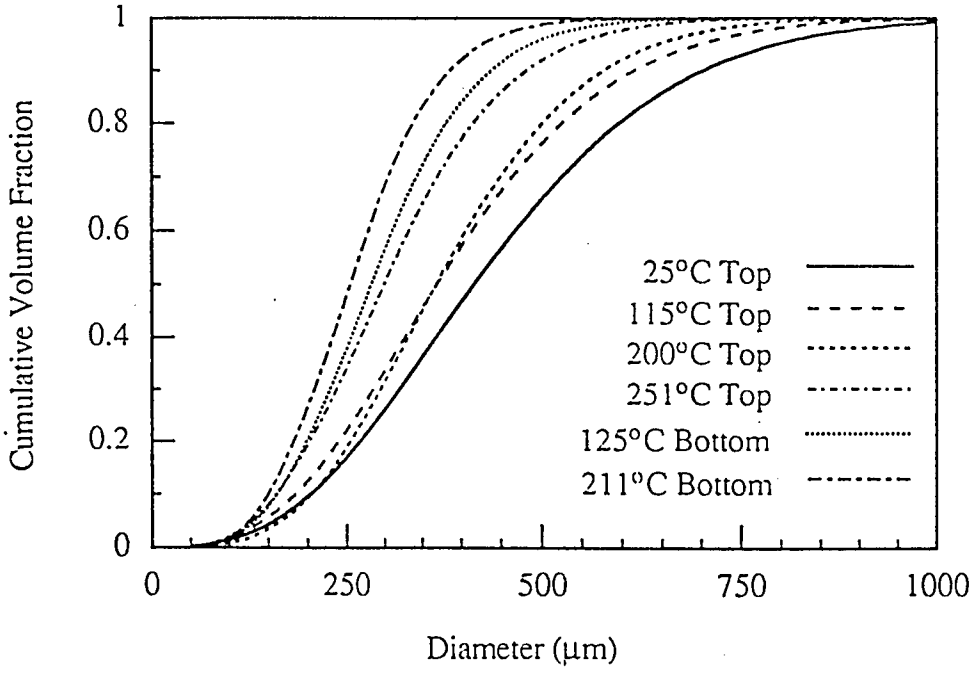

(a)

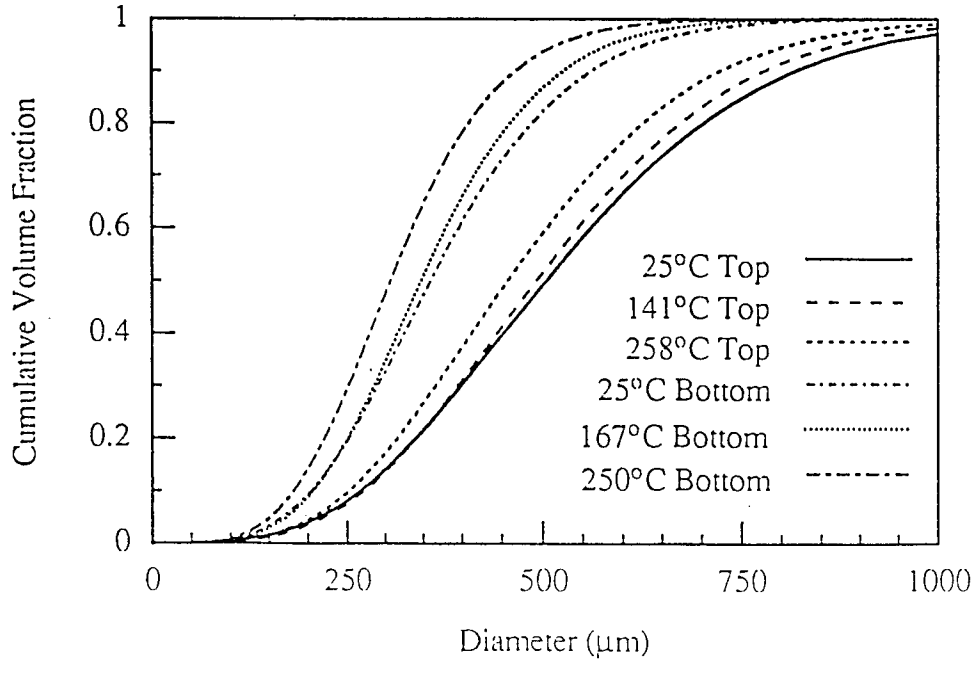

(b)

Figure 8. Cumulative volume data represented by the universal root-normal distribution for various regions and temperatures of impinging jet sprays of (a) ethanol and (b) water.

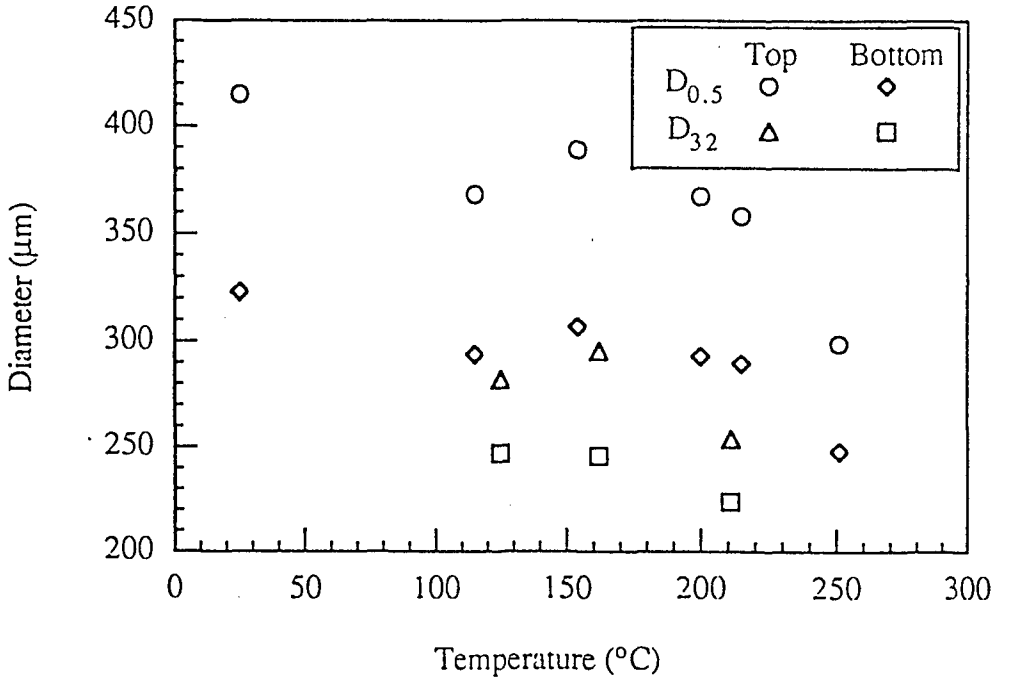

(a)

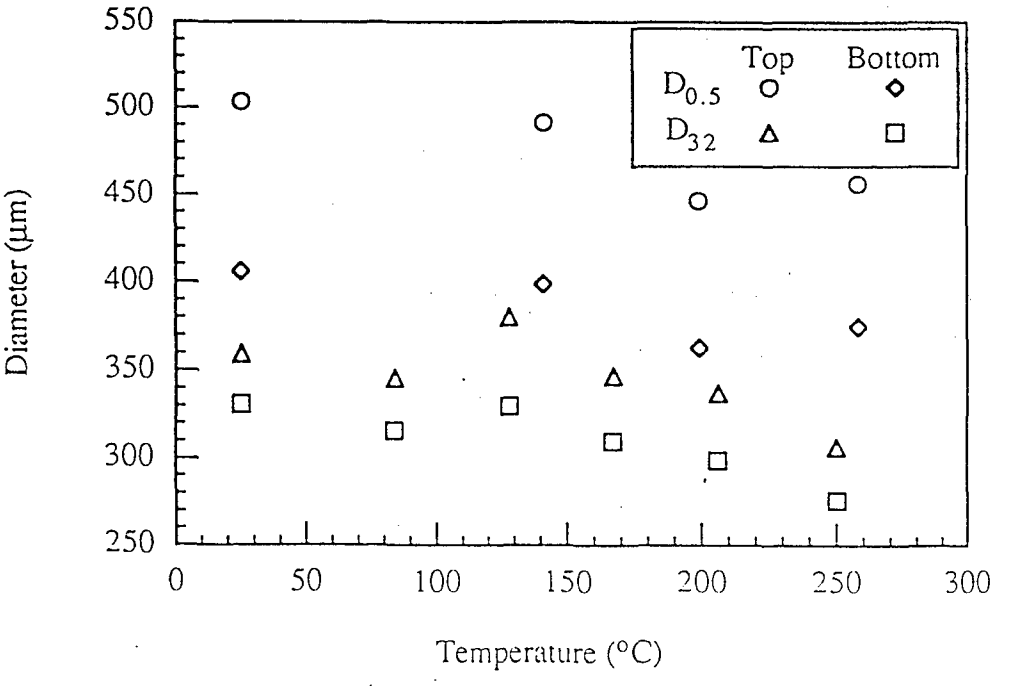

(b)

Figure 9. Variation of the Sauter mean diameter and the mass median diameter with temperature for impinging jet sprays of (a) ethanol and (b) water.

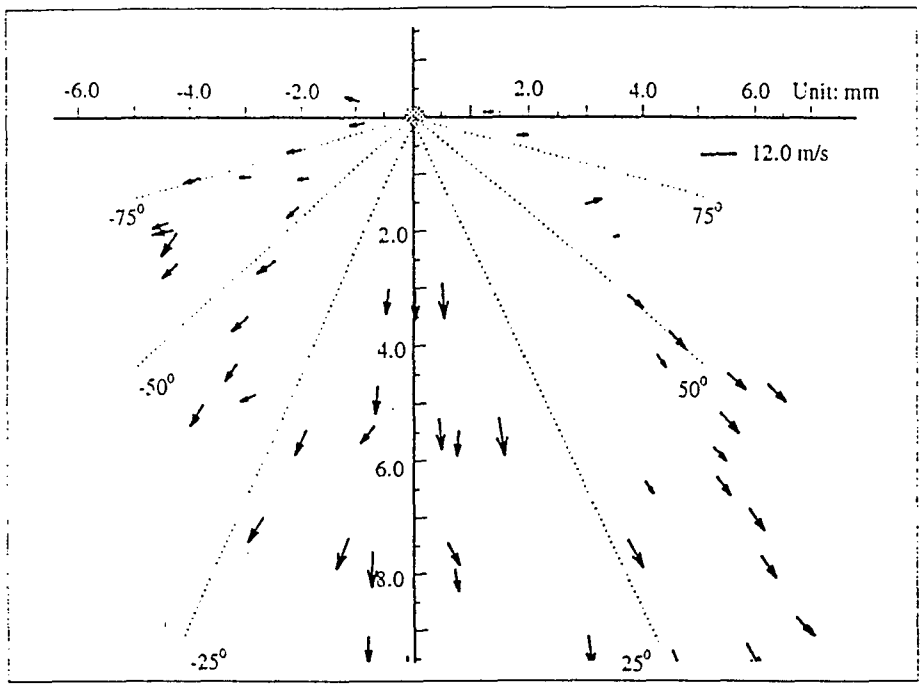

(a)

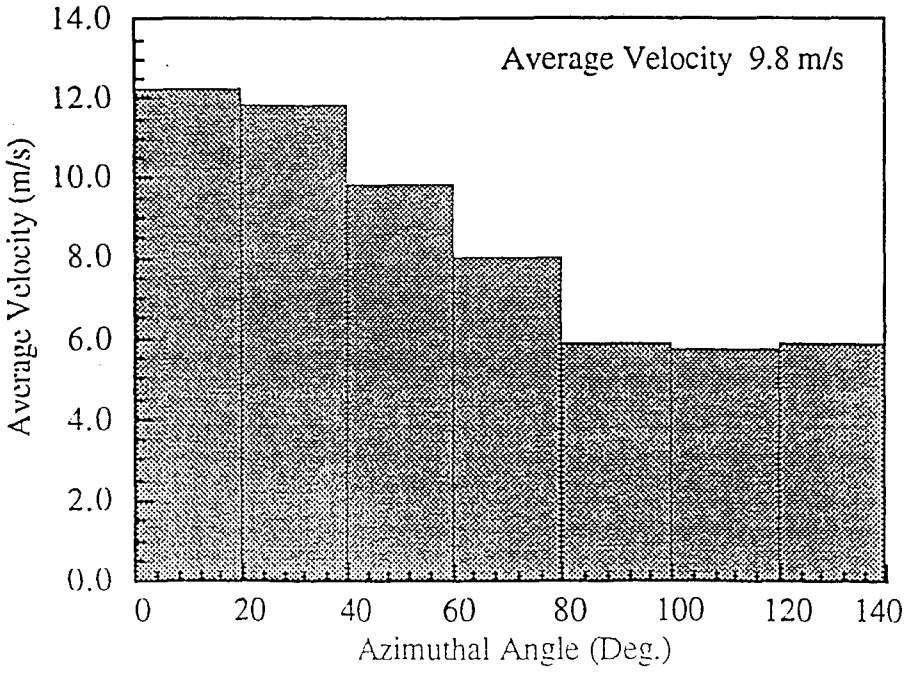

(b)

Figure 10 Holographic velocity analysis of dense region of ethanol spray: (a) measured velocity vector field, and (b) velocity distribution.

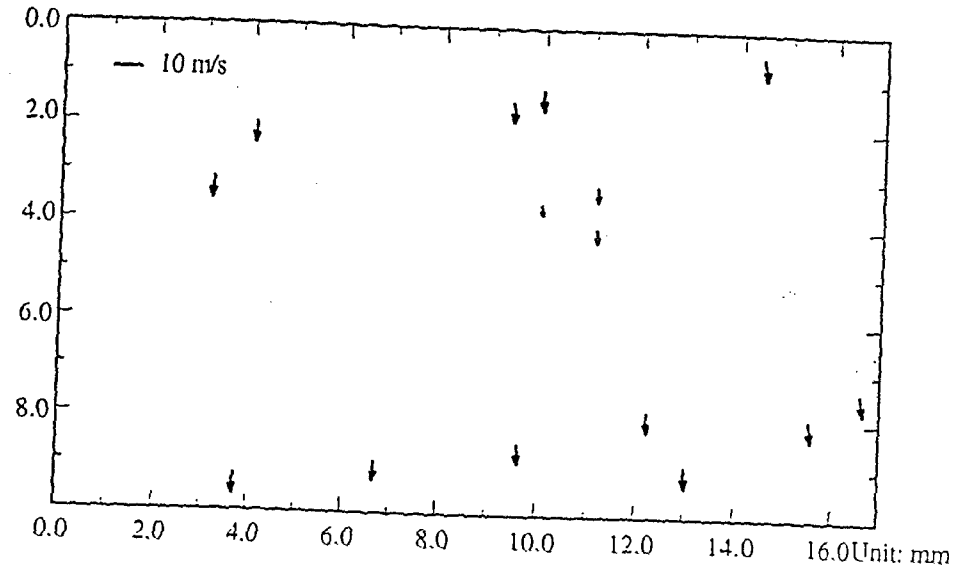

Figure 11 Holographic velocity analysis of bottom region of glycerol spray: measured velocity vector field.

LIST OF PROFESSIONAL PERSONNEL AND PUBLICATIONS

Publications in Refereed Journals

1. Y. Shen, C. Mitts and D. Poulikakos, "A Holographic Investigation on the Effect of Elevated Ambient Temperature on the Atomization Characteristics of Impinging Jet Sprays," *Atomization and Spray,* Vol. 6, 1997.

Graduate Students

1. Chad Mitts. Completed his *M.S. Thesis*, and graduated, Dec. 1996.